Numerical modeling of local capillary effects in porous media as a pressure discontinuity acting on the interface of a transient bi-fluid flow

Koloina Andriamananjara, Nicolas Moulin, Julien Bruchon, Pierre-Jacques Liotier, Sylvain Drapier

Numerical modeling of local capillary effects in porous media as a pressure discontinuity acting on the interface of a transient bi-fluid flow

K. Andriamananjara[a], N. Moulin[a], J. Bruchon[a,*], S. Drapier[a]

[a]*Hexcel - Mines Saint-Étienne Industrial Chair*
Mines Saint-Étienne, Univ Lyon, CNRS, UMR 5307 LGF, Centre SMS,
F-42023 Saint- Étienne cedex 2

Abstract

Transient flows through porous media can be controlled by local capillary forces. In an attempt to ease the representation of these complex multi-scale flows, this article presents a new numerical approach to account for these local forces, viewed as a global pressure discontinuity acting in bi-fluid flows through smeared-out porous media. A finite element discretization of the Darcy's equations is considered and a pressure enriched space is locally introduced at the fluid interface in order to capture the pressure discontinuity. Then, a Variational Multiscale Stabilization *(VMS)* method is selected to take into account the subgrid effects on the finite element solution and hence ensure the consistency of the finite element formulation. The fluid front is represented by a level set function, convected with the fluid velocity thanks to a finite element scheme stabilized with a Streamline-Upwind/Petrov-Galerkin *(SUPG)* method. Both convergence and implementation are first validated with the Method of Manufactured Solution *(MMS)* and the model shows a good convergence. Second, a comparison with experimental measurements in the case of capillary wicking of water into carbon reinforcements shows a very good correlation between experimental and numerical results.

Keywords: Capillary stress, Darcy's equations, stabilized finite element

*Corresponding author

Email addresses: andriamananjara@emse.fr (K. Andriamananjara), nmoulin@emse.fr (N. Moulin), bruchon@emse.fr (J. Bruchon), drapier@emse.fr (S. Drapier)

method, discontinuous pressure, capillary wicking

1. Introduction

Capillary effects define the ability of a liquid to maintain contact with a solid. They are localized and play a key role in the description of liquid flows in porous media. Their best visualization is the spontaneous wicking mechanisms, where the liquid flows without the assistance of any external force. Such phenomena are related in one hand to the surface tension between the liquid and the surrounding media such as air, and on the other hand, to the liquid-solid and air-solid surface energies.

During flows in a porous medium, micro- and macro-voids may develop following the competition between viscous and capillary effects. This work focuses on the capillary effects occurring in porous media such as fibrous reinforcements during infusion process, especially Liquid Resin Infusion (LRI) process. Indeed, capillary effects are traditionally neglected in the flow simulation during high pressure composite manufacturing processes. Meanwhile, experimental studies have shown that the capillary stress resulting from the interaction of carbon reinforcements and liquid, such as water or epoxy resin, can reach a value of $0.3 - 0.4$ bar in quasi-UD fabrics [62, 63], at the fibre scale [76] or in carbon woven fabrics [5]. This value represents approximatively one third of the 1 bar driving force available in the LRI process, which is too significant to be neglected and even permits to manufacture composite parts that could not be without its contribution. Consequently, the aim of this paper is to introduce these local capillary effects, in order to assess their influence on the filling stage scenarios at the scale of composite parts [46, 70].

Indeed, following the multi-scale nature of high performance composites, the study can be conducted at three different scales as shown in many studies [15, 22, 36, 60]: at the fiber or microscopic scale ($\sim 10^{-6}$m), at the tow or mesoscopic scale ($\sim 10^{-3}$m) and at the process or macroscopic scale ($\sim 10^{-1}$m). At microscopic scale, numerical modeling of the capillary rise is well-documented [11, 13, 52, 71]. Capillary effects are accounted for into Navier-Stokes or Stokes equations by the mean of the surface tensions between the three phases (solid-liquid-air) [4, 20, 24]. At mesoscopic scale, capillary effects are taken into account through the micro-diffusion within fiber tows. Generally, unsaturated flow models are adopted to describe this

problem. A sink term which depends on the capillary number is incorporated in the governing equations to model the capillary effects [65, 67, 72], but standing only for isotropic representations. In many research areas such as ground water infiltration or oil recovery, the capillary pressure is related to the saturation according to different analytical parameterizations such as the ones proposed by Van Genuchten, Stauffer, Kalaydjian, Hassanizadeh, Gray and Bareblatt [38, 47, 50].

This approach has been extended to composite manufacturing fields in order to simulate the filling stage and to assess void formation [17, 54, 59]. Capillary effects are usually represented through the introduction a single capillary pressure, although capillary effects do come from local mechanisms related to both orthotropic micro(meso)-structure architecture and surface tensions. Dedicated studies concentrate on these local phenomena [24] which are, for the moment, out of reach in tractable models at the structure scale. An alternative way of introducing these 3D effects at an upper scale is to consider their effect as a capillary stress tensor (3D representation) acting on the fluid-gas interface in a slug-flow approach, *i.e.* no saturation zone is considered at this scale. Accounting properly for the 3D pressure discontinuity in a numerical approach will allow to complete full models of infusion processes at the structure scale [15] including coupling with the wet/dry preform mechanical response, as well as to model dual-scale flows at the tow scale [75] provided an equivalent homogeneous medium can be used to represent populations of fibres. Notwithstanding any local effects related either to velocity or pressure fields which are of utmost interest to represent local physical changes, such as for shear-rate dependant fluids, void creations issues, or fluid pressure acting in wet preforms for coupling issues [22, 15].

In this work, an innovative macroscopic approach is adopted. The capillary action is described by a capillary stress tensor acting on the liquid-air interface. The subsequent jump of the pressure field at the flow front is taken into account numerically in the weak formulation of Darcy's equations. Those equations, established in a velocity-pressure mixed form, are solved using a Finite Element Method (FEM). Both velocity and pressure are approximated by continuous and linear fields. According to the Brezzi - Babuška theory, such an approximation is not stable. This issue is overcome by stabilizing the Finite Element (FE) formulation thanks to the Variational MultiScale (VMS) framework introduced by Hughes [39, 40] and extensively used and studied by Badia & Codina to stabilize Stokes', Darcy's and Maxwell's equations in a unified setting [7, 8, 9, 10]. However, a special attention is mandatory to

accurately capture the pressure discontinuity across the flow front, which is described here with a level-set method [57, 58, 69].

The literature provides several techniques to capture this local phenomenon. For instance, the Extended-Finite Element Method (X-FEM) [21, 32, 45] consists in enriching the pressure approximation space by discontinuous functions. This enrichment, which is not localized in the mesh elements, provides additional degrees of freedom, resulting in some computational issues when the discontinuity is moving (the mesh, and consequently the global "stiffness" matrix, need to be updated). A discontinuous Galerkin formulation [1, 12, 48, 56] can be another way of dealing with singular forces at the interface. As the continuity between elements is weakly imposed, it allows the solution to be discontinuous: each element has its own degrees of freedom and is connected to its neighboring by numerical fluxes. However, in our simulations, the interface does not necessarily correspond to edges of elements, but can cut these elements. In this work, the jump of pressure field is captured using the technique developed by Ausas *et al.* [6], which consists in a local enrichment of the pressure space by discontinuous functions. Unlike the X-FEM approach, the corresponding additional degrees of freedom are local to an interface element, and can therefore be eliminated at the elementary level before the final assembly.

The rest of this article is divided into four parts. Section 2 focuses on the mathematical description of the fluid flow problem, and the finite element strategy implemented. Section 3 describes the level-set method used to capture the fluid front, *i.e.* the interface across which pressure is discontinuous. An error analysis is given in Section 4 to assess the accuracy of the numerical developments. Finally, Section 5 compares simulation and experimental results for water capillary wicking in carbon reinforcements. Also, a 3D simulation of the resin flow through an orthotropic stiffener is carried out.

2. Fluid flow problem

2.1. Physical and mathematical description

Let Ω be a region of $\mathbb{R}^d$ (with $d = 2, 3$ the spatial dimension) bounded by $\partial\Omega$ (see Fig. 1). Ω represents a porous medium, the fibrous preform in our context, considered as an equivalent homogeneous orthotropic medium characterized by a porosity ϕ and a saturated permeability $\boldsymbol{K}$ independent on the fluid. The permeability is a measure indicating the capacity of the

material to allow fluids to pass through it. In a realistic description, the fibrous reinforcement is anisotropic and $\boldsymbol{K}$ is a symmetric tensor. The domain Ω is filled with two immiscible, Newtonian and incompressible fluids: a liquid of viscosity μ_l, occupying the subdomain Ω_l and a surrounding medium (for instance, the air) of viscosity $\mu_a \ll \mu_l$, occupying Ω_a. Hence: $\Omega = \Omega_l \cup \Omega_a$. The interface is denoted $\Gamma_{l/a}$: $\Gamma_{l/a} = \partial\Omega_l \cap \partial\Omega_a$.

The domain boundary $\partial\Omega$ is divided into two types of boundary: $\partial\Omega_D$ and $\partial\Omega_N$ such that $\partial\Omega = \partial\Omega_D \cup \partial\Omega_N$ and $\partial\Omega_D \cap \partial\Omega_N = \emptyset$, where respectively Dirichlet and Neumann boundary conditions are prescribed.

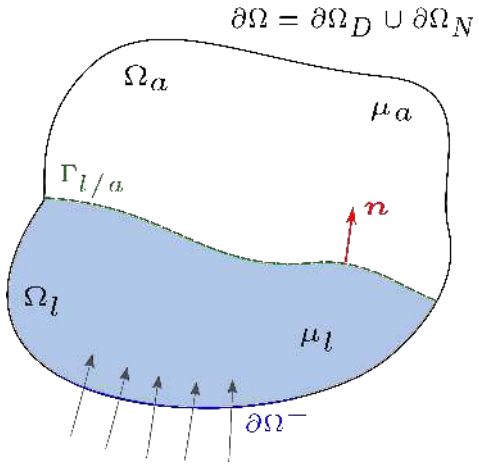

Figure 1: 2D-description of the domain Ω.

Darcy's equations [28] express the flow velocity $\boldsymbol{v}$ at the scale of the homogeneous equivalent medium, *i.e.* the superficial fluid velocity, with respect to the pressure gradient ∇p and two parameters: the fluid viscosity and the permeability (Eq. 1). The mass conservation is introduced through the divergence of the velocity $\boldsymbol{v}$ (Eq. 2). Hence, the governing equations are

$$\mu \boldsymbol{K}^{-1}\boldsymbol{v} + \nabla p = \boldsymbol{f}, \quad \mu = \begin{cases} \mu_l & \text{in} \quad \Omega_l \\ \mu_a & \text{in} \quad \Omega_a \end{cases} \tag{1}$$

$$\nabla \cdot \boldsymbol{v} = h \tag{2}$$

with $\boldsymbol{f}$ the external forces and h a source/sink term, equal to zero when the fluids are assumed to be incompressible. Assuming, for a while, that the axes of the orthonormal coordinate system $\{x, y, z\}$ coincide with the normals to the three symmetry planes of the orthotropic material, the permeability

tensor writes in this eigen-system:

$$\boldsymbol{K} = \boldsymbol{K}_{LOC} = \begin{pmatrix} K_x & 0 & 0 \\ 0 & K_y & 0 \\ 0 & 0 & K_z \end{pmatrix} \tag{3}$$

with $K_{\{x,y,z\}}$ the values of the permeability in the $x-$, $y-$ and $z-$directions, the index $_{LOC}$ refers to the local or material coordinate system.

The capillary effects are described at the macroscopic scale by a capillary stress tensor, $\boldsymbol{\sigma}_{cap}$, having the same eigen-directions as the permeability tensor, since they correspond to the symmetries of the orthotropic porous medium. Hence,

$$\boldsymbol{\sigma}_{cap} = \boldsymbol{\sigma}_{cap}^{LOC} = \begin{pmatrix} \sigma_{cap}^{x} & 0 & 0 \\ 0 & \sigma_{cap}^{y} & 0 \\ 0 & 0 & \sigma_{cap}^{z} \end{pmatrix} \tag{4}$$

with $\sigma_{cap}^{\{x,y,z\}}$ the components of the equivalent capillary stress at the interface $\Gamma_{l/a}$ in the $x-$, $y-$ and $z-$directions. In general situations, described in section 5.3, the eigen-directions of the previous tensors vary from point to point, and consequently, do not match with the axes of the global coordinate system. In this case, tensor $\boldsymbol{K}$ is expressed in the global system by: $\boldsymbol{K} = \boldsymbol{Q}\boldsymbol{K}_{LOC}\boldsymbol{Q}^{\boldsymbol{T}}$, where $\boldsymbol{Q}$ is the orthogonal tensor expressing the passage from the local to the global bases. Similarly, $\boldsymbol{\sigma}_{cap} = \boldsymbol{Q}\boldsymbol{\sigma}_{cap}^{LOC}\boldsymbol{Q}^{\boldsymbol{T}}$.

Capillary effects give rise to a jump of pressure across $\Gamma_{l/a}$. This jump, denoted $[p]$, is expressed as

$$[p] = \boldsymbol{n} \cdot \boldsymbol{\sigma}_{cap} \cdot \boldsymbol{n} \quad \text{on} \quad \Gamma_{l/a} \tag{5}$$

where $\boldsymbol{n}$ is the normal vector to the interface.

Finally, system (Eq. 1), (Eq. 2), completed by (Eq. 5), is closed by prescribing a normal velocity v_0 on $\partial\Omega_D$ and a pressure p_0 on $\partial\Omega_N$:

$$\boldsymbol{v} \cdot \boldsymbol{n} = v_0 \qquad \text{in } \partial\Omega_D \tag{6}$$

$$p = p_0 \qquad \text{in } \partial\Omega_N \tag{7}$$

$$[\boldsymbol{v} \cdot \boldsymbol{n}] = 0 \qquad \text{on } \Gamma_{l/a} \tag{8}$$

where the last condition (Eq. 8), the continuity of the normal velocity, expresses the mass conservation across the interface $\Gamma_{l/a}$.

2.2. Weak formulation

In order to solve the previous Darcy's system with a finite element method, the weak formulation of these equations has first to be established. Two approaches exist to express the weak formulation. First, the Darcy's problem can be formulated in pressure only, and the velocity post-calculated apart. However, mass conservation issues can appear when considering a jump of material properties such as a jump of permeability [29]. Second, and this is the strategy adopted here, a full velocity/pressure mixed weak formulation can be formulated, ensuring the mass conservation. Moreover, what is called the dual formulation of Darcy's equations [8, 34] is chosen, in order to naturally enforce the pressure discontinuity.

The dual variational formulation is obtained by multiplying the strong equations (Eq. 1) and (Eq. 2) respectively by any admissible and smooth enough velocity test function $\boldsymbol{w}$ and pressure test function q, and then by integrating by part the term $\boldsymbol{w}\cdot\nabla p$. The natural enforcement of the capillary stress results from this integration by parts:

$$\begin{aligned} < \boldsymbol{w}, \nabla p >_\Omega &= < \boldsymbol{w}, \nabla p >_{\Omega_l} + < \boldsymbol{w}, \nabla p >_{\Omega_a} \\ &= - < \nabla\cdot\boldsymbol{w}, p >_\Omega + < \boldsymbol{w}\cdot\boldsymbol{n}, [p] >_{\Gamma_{l/a}} + < \boldsymbol{w}\cdot\boldsymbol{n}, p >_{\partial\Omega_N} \\ &= - < \nabla\cdot\boldsymbol{w}, p >_\Omega + < \boldsymbol{w}\cdot\boldsymbol{n}, \boldsymbol{n}\cdot\boldsymbol{\sigma}_{cap}\cdot\boldsymbol{n} >_{\Gamma_{l/a}} + < \boldsymbol{w}\cdot\boldsymbol{n}, p_0 >_{\partial\Omega_N} \end{aligned}$$

where, for a bounded region R, the bilinear form $< .,. >_R$ denotes the $L^2(R)^n$ inner-product ($n = 1$ if a and b are scalars, $n = d$ if they are vectors): $< a, b >_R = \int_R a\cdot b\, dR$, for a and b in $L^2(R)^n$ the classical Lebesgues functional space,

$$L^2(R) = \{q : R \to \mathbb{R} \quad | \quad \int_R q^2\, dR < \infty\}$$

In order to complete the functional setting associated with the weak Darcy's equations, the Sobolev space $H(\nabla\cdot, \Omega)$ is also introduced:

$$H(\nabla\cdot, \Omega) = \{\boldsymbol{u} \in L^2(\Omega)^d \quad | \quad \nabla\cdot\boldsymbol{u} \in L^2(\Omega)\}$$

Finally, the dual formulation of the mixed Darcy system (Eq. 1) - (Eq. 2) - (Eq. 5) - (Eq. 6) reads: Find $(\boldsymbol{v}, p) \in H(\nabla\cdot, \Omega) \times L^2(\Omega)$, with $\boldsymbol{v}\cdot\boldsymbol{n} = v_0$ on $\partial\Omega_D$, such that

$$\begin{aligned} < \mu\boldsymbol{K}^{-1}\boldsymbol{v}, \boldsymbol{w} >_\Omega - < \nabla\cdot\boldsymbol{w}, p >_\Omega &= < \boldsymbol{f}, \boldsymbol{w} >_\Omega + < \boldsymbol{w}\cdot\boldsymbol{n}, p_0 >_{\partial\Omega_N} \\ &\quad + < \boldsymbol{w}\cdot\boldsymbol{n}, \boldsymbol{n}\cdot\boldsymbol{\sigma}_{cap}\cdot\boldsymbol{n} >_{\Gamma_{l/a}} \qquad (9) \\ < \nabla\cdot\boldsymbol{v}, q >_\Omega &= < h, q >_\Omega \qquad (10) \end{aligned}$$

$\forall(\boldsymbol{w}, q) \in H(\nabla\cdot, \Omega) \times L^2(\Omega)$, with $\boldsymbol{w}\cdot\boldsymbol{n} = 0$ on $\partial\Omega_D$, and $\mu = \mu_i$ in Ω_i.

2.3. Stabilized FE formulation

The computational domain Ω is discretized by using a mesh made up of triangles in 2D or tetrahedrons in 3D. Let Ω_h be this discretized domain. The velocity $\boldsymbol{v}$ and the pressure p are approximated by $\boldsymbol{v_h}$ and p_h, which are both continuous and piecewise linear functions ($P1/P1$ approximation). However, such an approximation is not stable [8, 3, 29] according to Ladysenskaya-Brezzi-Babuška theory. In this work, this difficulty is overcome by using a Variational Multi-Scale (VMS) technique [8, 40] consisting in adding some stabilization terms to the Galerkin formulation. More precisely, the velocity and pressure functional spaces, $\mathcal{V} \equiv H(\nabla\cdot, \Omega)$ and $\mathcal{P} \equiv L^2(\Omega)$ are split as

$$\mathcal{V} = \mathcal{V}_h \otimes \mathcal{V}' \quad \text{and} \quad \mathcal{P} = \mathcal{P}_h \otimes \mathcal{P}'$$

where $\mathcal{V}_h$ and $\mathcal{P}_h$ are the velocity and pressure finite element spaces and $\mathcal{V}'$ and $\mathcal{P}'$ are the so-called subgrid or unresolvable scale spaces of velocity and pressure. Following this approach, the solution $(\boldsymbol{v}, p)$ of the variational problem (Eq. 9)-(Eq. 10), as well as the test functions $(\boldsymbol{w}, q)$ are divided as

$$\begin{aligned} \boldsymbol{v} &= \boldsymbol{v_h} + \boldsymbol{v'}, \quad p &= p_h + p' \\ \boldsymbol{w} &= \boldsymbol{w_h} + \boldsymbol{w'}, \quad q &= q_h + q' \end{aligned}$$

Subsequently, the variational problem is broken down into a problem at the resolvable scale, the finite element problem, and a subgrid scale problem, which cannot be explicitly solved. Consequently, the strategy of VMS methods consists in approximating the effects of the subgrid scale onto the finite element scale, leading to additional terms in the finite element formulation. In this work, the Algebraic SubGrid Scale (ASGS) technique is used, a subtype of VMS method developed by Badia and Codina in [8, 9, 25, 37]. The subgrid terms are expressed as a function of the finite element residual such that, on a mesh element e

$$\boldsymbol{v'}_{|e} \approx -\boldsymbol{\tau_u}^e(\mu \boldsymbol{K}^{-1}\boldsymbol{v_h} + \nabla p_h - \boldsymbol{f})_{|e} \tag{11}$$

$$p'_{|e} \approx -\tau_p^e(\nabla\cdot\boldsymbol{v_h} - h)_{|e} \tag{12}$$

where $\boldsymbol{\tau_u}^e$ and τ_p^e are stabilization parameters (Eq. 13) on the element e. They depend on the mesh size h_e, the geometry (through L_0, a characteristic length of the domain Ω), the fluid viscosity, the porous medium permeability and the stabilization coefficients c_u and c_p (in this work, $c_u = c_p = 1$). As we

are using $P1/P1$ approximation, these two parameters are expressed as [2, 8]:

$$\boldsymbol{\tau_u}^e = \frac{h_e \boldsymbol{K}_{|\boldsymbol{e}}}{c_u L_0 \mu_{|e}}, \quad \tau_p^e = \frac{\mu_{|e} c_p L_0 h_e}{K_{m|e}} \tag{13}$$

with K_m^e an equivalent permeability, chosen as [15]

$$K_m^e = \frac{1}{d} trace(\boldsymbol{K}_{|e})$$

Including the subgrid scale effects, the discrete FE system reads: Find $(\boldsymbol{v_h}, p_h) \in \mathcal{V}_h \times \mathcal{P}_h$, with $\boldsymbol{v_h} \cdot \boldsymbol{n} = v_0$ on $\partial\Omega_{hD}$, such that

$$\begin{aligned}
&< \mu \boldsymbol{K^{-1}} \boldsymbol{v_h}, \boldsymbol{w_h} >_{\Omega_h} - < \nabla \cdot \boldsymbol{w_h}, p_h >_{\Omega_h} - < \nabla \cdot \boldsymbol{v_h}, q_h >_{\Omega_h} \\
&+ \sum_e \tau_p^e < \nabla \cdot \boldsymbol{v_h}, \nabla \cdot \boldsymbol{w_h} >_e + \sum_e \boldsymbol{\tau_u}^e < -\mu \boldsymbol{K^{-1}} \boldsymbol{v_h} - \nabla p_h, \mu \boldsymbol{K^{-1}} \boldsymbol{w_h} + \nabla q_h >_e \\
&=< \boldsymbol{w_h} \cdot \boldsymbol{n}, \boldsymbol{n} \cdot \boldsymbol{\sigma_{cap}} \cdot \boldsymbol{n} >_{\Gamma_{hl/a}} + < \boldsymbol{w_h} \cdot \boldsymbol{n}, p_0 >_{\partial\Omega_{hN}} + < \boldsymbol{f}, \boldsymbol{w_h} >_{\Omega_h} + < h, q_h >_{\Omega_h} \\
&+ \sum_e \boldsymbol{\tau_u}^e < \boldsymbol{f}, \mu \boldsymbol{K^{-1}} \boldsymbol{w_h} + \nabla q_h >_e + \sum_e \tau_p^e < h, -\nabla \cdot \boldsymbol{w_h} >_e
\end{aligned} \tag{14}$$

$\forall (\boldsymbol{w_h}, q_h) \in \mathcal{V}_h \times \mathcal{P}_h$ with $\boldsymbol{w_h} \cdot \boldsymbol{n} = 0$ on $\partial\Omega_{hD}$. In this formulation, $\sum_e$ stands for the summation over all the mesh elements e.

Note that when the porous medium is assumed to be isotropic, previous formulation (Eq. 14) can be slightly simplified, since the permeability $\boldsymbol{K}$, the stabilization parameter $\boldsymbol{\tau_u}$ and the capillary stress become scalar.

2.4. Pressure discontinuity

The capillary stress generates a pressure discontinuity at the liquid/air interface. Moreover, for two different liquids the jump of viscosity across this same interface leads to a discontinuity of the pressure gradient. In a FE framework, these two kinds of discontinuities represent a numerical difficulty to be dealt with. A first approach found in the literature consists in circumventing the discontinuity by considering a smooth transition area around the interface [16]. The performance of this method depends strongly on the smoothing function, on the transition region thickness, and consequently on the local mesh size [27]. Since no mesh adaptation strategy is used in this work, the liquid-air interface will be identified by a continuous set of segments (2D) or triangles (3D) crossing the mesh elements [15, 61] and built locally thanks to the level-set front-capturing method described in Section 3.

This approach allows to integrate the capillary term into (Eq. 14) directly on a segment or triangle, using one integration point if the capillary stress is piecewise constant. Moreover, additional integration points are considered in the elements e crossed by the interface, in order to evaluate accurately the term $< \mu \boldsymbol{K}^{-1} \boldsymbol{v_h}, \boldsymbol{w_h} >_e$. Thus, in the 2D configuration (Fig. 2), assuming that both viscosities of the liquid and air are constant, 3 integrations points are used in each sub-element deriving from the element split.

However, such a split is not sufficient to ensure the accurate capture of the pressure and pressure gradient discontinuities. Especially, continuous and piecewise linear approximation of the pressure, piecewise linear approximation of the interface, give rise to the parasitic current phenomenon (even if the curvature is not involved in the equations), which consists in spurious oscillations of the velocity, possibly deteriorating the interface [33]. Here again, several options are available in the literature to reduce these oscillations [23, 30, 55]. In particular, an enrichment of the pressure space [6, 20, 26, 42, 43, 44] can be set up, locally in the elements crossed by the fluid front. This work considers the pressure enrichment developed by R. Ausas *et al.* [6]. Originally introduced to deal with discontinuities involved in Navier-Stokes equations, this technique is applied here to Darcy's equations. This consists in adding, in the elements crossed by the interface, the two discontinuous shape functions M_1 and M_2 described in Fig. 2 and derived as following:

$$M_1(\boldsymbol{x}) = (1 - S(\boldsymbol{x}))\chi^l(\boldsymbol{x}) \quad (15)$$

$$M_2(\boldsymbol{x}) = S(\boldsymbol{x})\chi^a(\boldsymbol{x}) \quad (16)$$

with

$$S(\boldsymbol{x}) = \sum_{J \in \mathcal{J}^a} N_J(\boldsymbol{x}) \quad (17)$$

where N_J is the usual linear shape function associated with node J, χ^l is equal to 1 in the liquid region, to 0 elsewhere, and $\chi^a = 1 - \chi^l$. The set $\mathcal{J}^a$ corresponds to the element nodes being in Ω_a.

In such elements, the pressure field p_h is expressed as

$$p_h(\boldsymbol{x}) = \sum_J P_J N_J(\boldsymbol{x}) + C_1 M_1(\boldsymbol{x}) + C_2 M_2(\boldsymbol{x}) \quad (18)$$

where P_J are the degree of freedom associated with the element vertices J, while C_1 and C_2 are those associated with the discontinuous shape functions

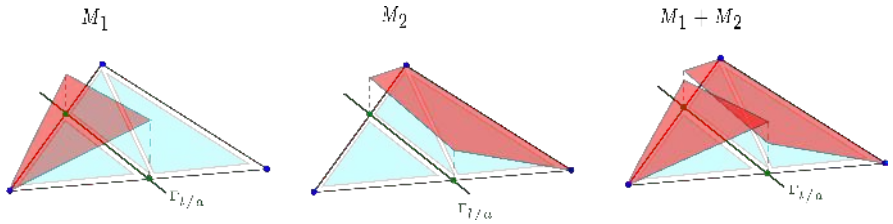

Figure 2: 2D local pressure enrichment and surface reconstruction (inspired of [6]).

M_1 and M_2. However, since C_1 and C_2 are defined per element, they can be eliminated by static condensation, at the elementary level, prior to the final assembly. Therefore, the main advantage of combining the interface reconstruction and local pressure enrichment is that the discontinuity generated by the capillary stress is treated without increasing the number of final degrees of freedom and affecting the computation time.

3. Fluid front capturing: level-set method

The moving flow front is captured by a level-set method [57, 69], consisting in choosing a continuous function, the so-called level-set function, $\psi(\boldsymbol{x}, t) : \Omega \times \mathbb{R}^+ \to \mathbb{R}$, negative in Ω_l and positive in Ω_a. Consequently, the interface $\Gamma_{l/a}$ is implicitly described as the zero-isovalue of function ψ:

$$\Gamma_{l/a}(t) = \{\boldsymbol{x} \in \Omega \quad | \quad \psi(\boldsymbol{x}, t) = 0\} \tag{19}$$

where t denotes the time variable. Note that the gradient of ψ allows the computation of the normal vector normal at the interface.

Assuming the flow velocity $\boldsymbol{v}$, defined both in Ω_l and Ω_a, known at each instant $t \in [0, T]$ (T is the final time of the simulation), the level-set function is then convected according to the hyperbolic equation (Eq. 20):

$$\frac{\partial \psi}{\partial t} + \boldsymbol{v} \cdot \nabla \psi = 0 \quad \forall (\boldsymbol{x}, t) \in \Omega \times [0, T] \tag{20}$$

$$\psi(\boldsymbol{x}, t = 0) = \psi_0 \quad \forall \boldsymbol{x} \in \Omega \tag{21}$$

$$\psi(\boldsymbol{x}, t) = g(\boldsymbol{x}, t) \quad \forall (\boldsymbol{x}, t) \in \partial\Omega^- \times [0, T] \tag{22}$$

where $g(\boldsymbol{x}, t)$ (Eq. 22) corresponds to the value of ψ to be imposed on the incoming boundary $\partial\Omega^-$ (Fig. 1)

$$\partial\Omega^-(t) = \{\boldsymbol{x} \in \partial\Omega \quad | \quad \boldsymbol{v}(\boldsymbol{x}, t) \cdot \boldsymbol{n} < 0\},$$

while (Eq. 21) states for the initial condition at $t = 0$.

3.1. SUPG formulation

Transport equation (Eq. 20) is solved by a FE technique, using the same mesh as for Darcy's equations. The variational formulation is first obtained by multiplying (Eq. 20) by any admissible and smooth enough test function and integrating the product over Ω. The time interval is discretized by a set of points $0 = t_0 < t_1 < \cdots < t_n < t_{n+1} < \cdots < t_N$, and a finite difference scheme in time, the implicit Crank-Nicholson scheme, is then applied to (Eq. 20). It results that at each instant t_n, $\psi(\cdot, t_n)$ is approximated by $\psi_h(\cdot, t_n)$ a continuous piecewise linear function. However, the usual Galerkin approach is known to be not stable for hyperbolic equations. This issue can be avoided by considering a Streamline Upwind Petrov-Galerkin (SUPG) method, introduced by Hughes in [19], and consisting in taking the test functions in a space different of the shape functions. More precisely, shape functions are still the nodal functions N_J already introduced, but the test functions, denoted N_J^*, are now defined on a mesh element e, as

$$N_J^* = N_J + \tau^e \boldsymbol{v} \cdot \boldsymbol{\nabla} N_J$$

where the stabilization parameter τ^e is chosen as

$$\tau^e = \frac{1}{2}\frac{h_e}{v_e}$$

with h_e the size of element e and v_e the norm of the average velocity in e.

This modification of the test functions adds, in a consistent way, an upwind artificial diffusion term stabilizing the FE formulation, at least as long as the convective term remains under control.

3.2. Filtered level-set

For the level-set procedure described below to be effective, the level-set function ψ has to be initialized with a specific expression. Let $d_0(\boldsymbol{x})$ denote the signed distance function from point $\boldsymbol{x}$ to the initial liquid-air interface $\Gamma_{la}(0)$. The initial expression of the level-set function, involved in the initial condition (Eq. 21) is then chosen as

$$\psi_0(\boldsymbol{x}) = \varepsilon \tanh\left(\frac{d_0(\boldsymbol{x})}{\varepsilon}\right) \tag{23}$$

where ε can be viewed as the thickness of the interface. In practice: $\varepsilon = 3h_e$.

Outside a narrow band around the interface, ψ_0 quickly tends towards the constant values $\pm\varepsilon$. Therefore, condition (Eq. 22) to be prescribed on the inflow boundary can easily be enforced. Additionally, within this tiny band close to the interface, ψ_0 is equal, in the first order, to the distance function d_0. A distance function have, by definition, a unit gradient: $\| \nabla d_0 \| = 1$. This property ensures the "control" of the convection term in transport equation (Eq. 20) and thus the efficiency of the SUPG stabilization. However, the initial "tanh-like" shape (Eq. 23) is not preserved under the transport of ψ with the Darcy's velocity field $\boldsymbol{v}$. That is why, as this velocity varies abruptly (but continuously) through the liquid-air interface, steep gradients of level-set function will develop in its vicinity, and the SUPG stabilization will fail. This problem is avoided by periodically reinitializing the level-set function: the zero-isovalue is preserved, while the tanh property is applied elsewhere. Based on the relation $d\tanh(x)/dx = 1 - \tanh^2(x)$, function ψ is of the form (Eq. 23) if

$$\| \nabla \psi \| = \left| 1 - \left(\frac{\psi}{\varepsilon} \right)^2 \right| \tag{24}$$

At a given time t_n, the reinitialization step consists in solving iteratively the Hamilton-Jacobi equation

$$\frac{\partial \tilde{\psi}}{\partial \tau} + sgn(\tilde{\psi}) \left(\| \nabla \tilde{\psi} \| - \left| 1 - \left(\frac{\tilde{\psi}}{\varepsilon} \right)^2 \right| \right) = 0 \tag{25}$$

$$\tilde{\psi}(x, \tau = 0) = \psi(x, t_n) \tag{26}$$

until reaching the steady state, *i.e.* $\partial \tilde{\psi} / \partial \tau = 0$, corresponding consequently to the property (Eq. 24). This state gives the reinitialized level-set function. In practice, only a few increments (3 in our simulations) are necessary to recover the unit gradient property in the narrow band around the interface. In (Eq. 25), τ is a time-like variable, and sgn is the regularized sign function [57]

$$sgn(\psi) = \frac{\psi}{\sqrt{\psi^2 + \| \nabla \psi \|^2 h_e^2}} \tag{27}$$

Note that, classically, Hamilton-Jacobi equation (Eq. 25) can be considered as a transport equation with a right-hand-side, and is then solved in the same way as the level-set convection equation (Eq. 20). The reinitialization

velocity is equal to $sgn(\psi)\frac{\nabla\tilde{\psi}}{\|\nabla\tilde{\psi}\|}$, while the non-linear terms are explicitly evaluated at the previous iteration.

3.3. Time-stepping strategy

The time-stepping strategy consists, for a given time increment, in solving Darcy's equations, then updating the flow front position by solving the level-set transport equation using the Darcy's velocity, and moving on to the next time increment. To sum up, the algorithm coupling Darcy's and level-set problems is as following:

Algorithm 1 Staggered algorithm for Darcy's and level-set problems

Require: $\psi(\boldsymbol{x}, t=0) = \psi_0$ the initial value for the level set function
  while $0 < t^{n+1} < T$ **do**
    1- Fluid problem:
    Find $(\boldsymbol{v_h}, p_h) \in \mathcal{V}_h \times \mathcal{P}_h$ by solving Darcy's equations (Eq. 14)
    2- Flow front problem:
    Find ψ_h by solving the level-set equations
    3- Reinitialization problem:
    Repeat 3 times: Solving Hamilton-Jacobi's equations (Eq. 25)
  end while

4. Convergence analysis

The FE model presented in the previous section has been implemented in the FE software Z-set [68]. The efficiency of the implementation, as well as the accuracy of the approach, are evaluated by an error analysis based on the Method of Manufactured Solutions (MMS) [64]. This consists in selecting velocity and pressure fields that satisfy Darcy's equations (Eq. 1)-(Eq. 2) and calculating the corresponding right-hand-side terms that are then prescribed in the FE problem. Performance of the implementation measures the capability of reproducing the initial fields.

The 2D-computational domain is the unit square $\Omega = [0,1] \times [0,1]$. The analytical pressure field is defined as

$$p(x,y) = \begin{cases} \sin(2\pi x)\sin(2\pi y) & \text{for} \quad y < \frac{1}{2} \\ \sin(2\pi x)\sin(2\pi y) + \sigma_{cap} & \text{for} \quad y > \frac{1}{2} \end{cases} \tag{28}$$

with σ_{cap} the scalar value of the capillary stress in the isotropic case.

Replacing (Eq. 28) inside Darcy's equation (Eq. 1) gives the components of the velocity, v_x and v_y

$$\begin{aligned} v_x &= \frac{K}{\mu} 2\pi \cos(2\pi x)\sin(2\pi y) \\ v_y &= \frac{K}{\mu} 2\pi \sin(2\pi x)\cos(2\pi y) \end{aligned} \tag{29}$$

These fields (Eq. 28) and (Eq. 29) satisfy Darcy's system (Eq. 1)-(Eq. 2) with the term h taken as

$$h = \nabla \cdot \boldsymbol{v} = \frac{K}{\mu} 8\pi^2 \sin(2\pi x)\sin(2\pi y) \tag{30}$$

Only one type of boundary condition is considered here, the Dirichlet one (Eq. 6): $\boldsymbol{v} \cdot \boldsymbol{n} = v_0 = 0$ on $\partial\Omega$. Thus, the so-called compatibility condition is fulfilled, that is

$$\int_\Omega \nabla \cdot \boldsymbol{v}\, d\Omega = \int_{\partial\Omega} \boldsymbol{v} \cdot \boldsymbol{n}\, d\Gamma = \int_{\partial\Omega} v_0\, d\Gamma = 0$$

In all the simulations shown in this section, the pressure jump across the line $\{y = \frac{1}{2}\}$ is equal to 1, $[p] = \sigma_{cap} = 1$, while the ratio K/μ is also unit (isotropic case). Pressure and velocity obtained by the FE strategy described before are plotted in a 3D-representation in Fig. 3 using an unstructured mesh of element size $h_e = 0.0125$. The pressure discontinuity is well-captured, without apparent oscillations of pressure. This is qualitatively confirmed in Fig. 4, where the computed pressure is satisfactorily compared to the analytical one along two lines, $\{x = \frac{1}{4}\}$ and $\{x = \frac{1}{2}\}$.

Next, a quantitative analysis of the error made on velocity and pressure is performed by considering 4 structured meshes of size, respectively, $h_e = 1/20$, $1/40$, $1/80$ and $1/160$. On each of these meshes, pressure error is calculated with the usual L^2-norm denoted $\|\cdot\|_{L^2}$, while velocity error is estimated both in L^2-norm and in $H(\nabla\cdot)$-norm denoted $\|\cdot\|_{H(\nabla\cdot)}$ (Eq. 31):

$$\|u\|_{L^2} = \left(\int_\Omega u^2 d\Omega\right)^{\frac{1}{2}}, \quad \|u\|_{H(\nabla\cdot)} = \left(\|u\|_{L^2}^2 + \|\nabla \cdot u\|_{L^2}^2\right)^{\frac{1}{2}} \tag{31}$$

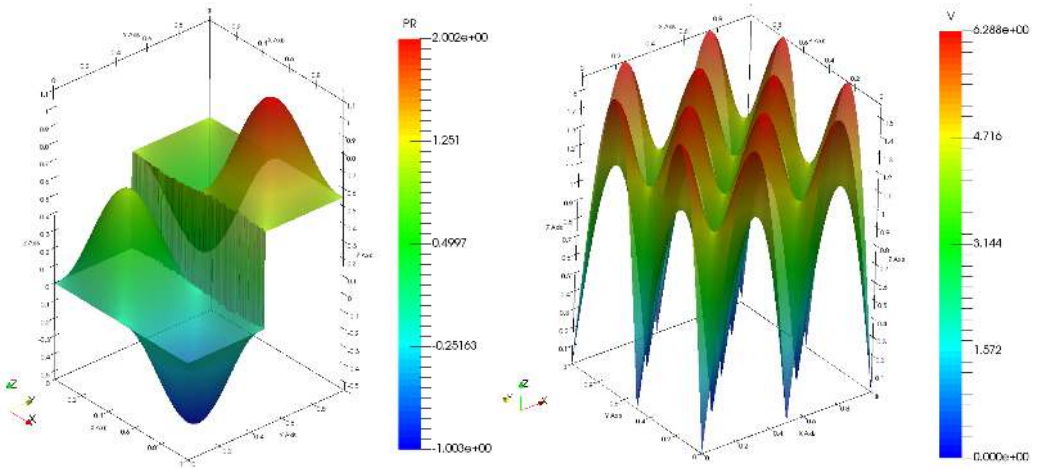

(a) Pressure (b) Velocity

Figure 3: 3D-plot of pressure and velocity fields (Eq. 28)-(Eq. 29), obtained by the FE solution.

The theoretical convergence rates, without discontinuity of pressure, are 2 in L^2-norm both for the pressure and velocity, and 1 in the $H(\nabla\cdot)$-norm for the velocity [3, 8, 53]. Therefore, three different cases are proposed here: a continuous case, corresponding to $\sigma_{cap} = 0$, in order to assess the Darcy's solver in a classical situation and have a reference situation; two discontinuous cases with $\sigma_{cap} = 1$ as mentioned above, but one without pressure enrichment of Section 2.4, and one with this technique. Results are summarized in Tables 1-2-3 and Fig. 5.

Mesh	h_e	$\|p - p_h\|_{L^2}$	$\|\boldsymbol{v} - \boldsymbol{v_h}\|_{L^2}$	$\|\boldsymbol{v} - \boldsymbol{v_h}\|_{H(\nabla\cdot)}$
20×20	0.05	0.0213803	0.0839136	6.76775
40×40	0.025	0.00389416	0.0188836	3.3258
80×80	0.0125	0.000714466	0.00416498	1.61289
160×160	$6.25 \cdot 10^{-3}$	0.000148175	0.00100372	0.812385

Table 1: Error in the L^2-norm for the pressure, and both the L^2-norm and $H(\nabla\cdot)$-norm for the velocity. Case with a continuous pressure.

We observe that without pressure discontinuity, the convergence rate obtained is in agreement with the optimal one, since the rate is slightly higher

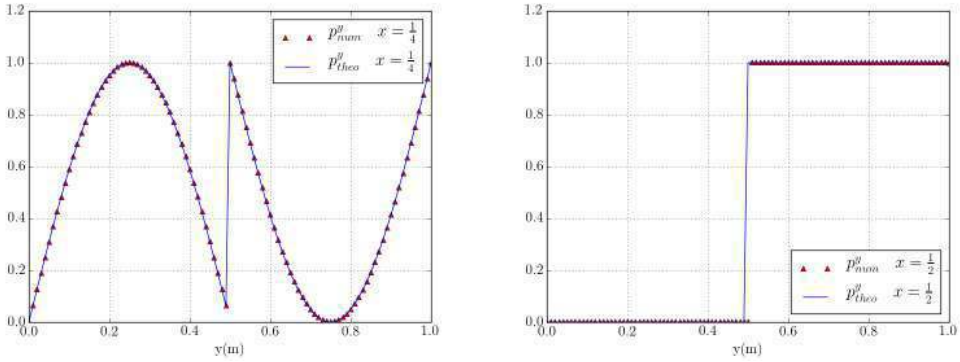

(a) $x = \frac{1}{4}$ (b) $x = \frac{1}{2}$

Figure 4: Comparison between analytical pressure field (Eq. 28) (continuous line) and results of simulation (dots), along the lines $x = \frac{1}{4}$ and $x = \frac{1}{2}$.

Mesh	h_e	$\|p - p_h\|_{L^2}$	$\|\boldsymbol{v} - \boldsymbol{v_h}\|_{L^2}$	$\|\boldsymbol{v} - \boldsymbol{v_h}\|_{H(\nabla\cdot)}$
20×20	0.05	0.0889837	0.109918	7.2842
40×40	0.025	0.0475362	0.0203123	3.33272
80×80	0.0125	0.0367567	0.00888546	2.1614
160×160	$6.25 \cdot 10^{-3}$	0.0231142	0.00189264	0.906225

Table 2: Error in the L^2-norm for the pressure, and both the L^2-norm and $H(\nabla\cdot)$-norm for the velocity. Case with pressure discontinuity and no pressure enrichment.

Mesh	h_e	$\|p - p_h\|_{L^2}$	$\|\boldsymbol{v} - \boldsymbol{v_h}\|_{L^2}$	$\|\boldsymbol{v} - \boldsymbol{v_h}\|_{H(\nabla\cdot)}$
20×20	0.05	0.0615517	0.0933167	6.94098
40×40	0.025	0.0211956	0.0247864	3.63211
80×80	0.0125	0.00571188	0.00801094	1.9443
160×160	$6.25 \cdot 10^{-3}$	0.00237119	0.00323276	1.55267

Table 3: Error in the L^2-norm for the pressure, and both the L^2-norm and $H(\nabla\cdot)$-norm for the velocity. Case with pressure discontinuity and local pressure enrichment.

than 2 for both pressure and velocity in L^2-norm, and equal to 1 for the velocity in $H(\nabla\cdot)$-norm. As expected, the two cases with pressure discontinuity let show lower convergence rates compared to the continuous case, especially for the pressure. Without enrichment strategy, a sub-optimal convergence rate

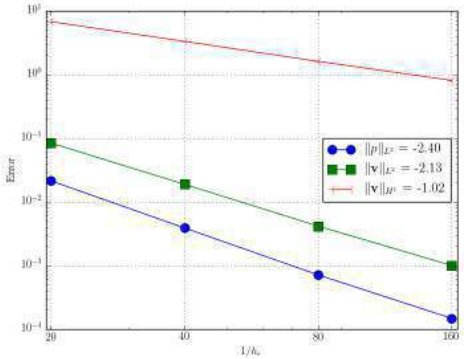

(a)

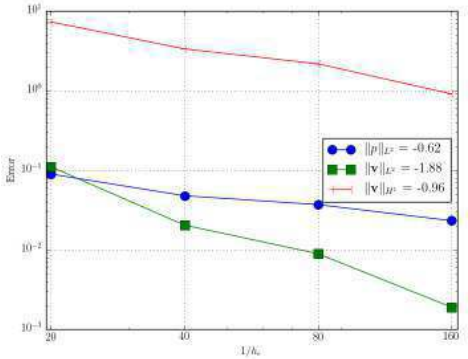

(b)

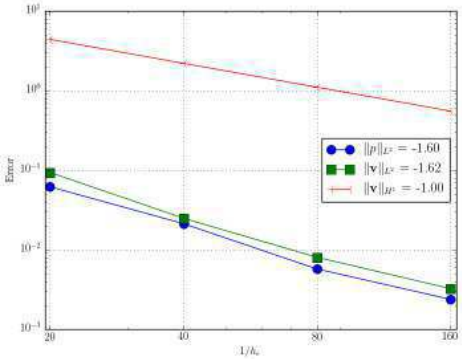

(c)

Figure 5: Error analysis: continuous case (a), discontinuous case without pressure enrichment (b) and discontinuous case with local pressure enrichment (c).

of 0.62 is obtained for pressure, corresponding to approximatively 1/3 of the theoretical order predicted for the continuous case. However, when enriching locally the pressure space, this rate is greatly improved, since jumping up to 80% of this same theoretical order, with the value of 1.6. Note that, with this same enrichment technique, but considered in the context of Navier-Stokes equations, Ausas and co-authors [6] obtained a pressure convergence rate equal to 75% of the one predicted with a continuous pressure. Hence, we can conclude that the numerical approach presented below allow us to describe with accuracy the pressure discontinuity when solving the Darcy's equations with a capillary stress applied on the moving flow front.

5. Numerical applications

This section assesses and demonstrates the performance of our numerical model in realistic contexts. First, numerical simulations of flows through porous media with a very low permeability are carried out, and the interest of local pressure enrichment is highlighted. Next, capillary wicking simulations are performed and the results are compared with experimental studies. Finally, a first approach of flows in 3D orthotropic materials is provided through the simulation of the filling stage of a T-stiffener during a LRI process. It is also used to demonstrate that simply shifting the pressure at a boundary condition by the capillary stress may hold for UD cases, but is not satisfactory in terms of filling scenario and results for general 3D cases.

5.1. Ascending capillary flow and realistic parameters

The numerical strategy is assessed by simulating a unidirectional flow in a porous medium with realistic properties, in terms of permeabilities, viscosities and capillary stresses, in the context of composite materials manufacturing. Thus, the computational domain Ω is a square of 1 meter side. The isotropic permeability K is equal to $3.0 \times 10^{-13}\mathrm{m}^2$, while the isotropic capillary stress, applied on the interface $\Gamma_{l/a} \equiv \{y = h = 1/2\}$, is of 32×10^3 Pa. Viscosities are $\mu_l = 10^{-3} Pa.s$ and $\mu_a = 10^{-5} Pa.s$ This pressure is the only driving force, since boundary conditions on both planes $\{y = 0\}$ and $\{y = 1\}$ are set to the atmospheric pressure. The remaining boundaries are considered as impervious walls, thus the $\boldsymbol{v} \cdot \boldsymbol{n} = 0$ condition is applied on the vertical edges of the domain, $\{x = 0\}$ and $\{x = 1\}$. All numerical values of material properties and boundary conditions are sum up in Fig. 6.

In the case of a unidirectional flow, the analytical solution of Darcy's equations is quite simple to determine. Indeed, the pressure is piecewise linear, while the velocity is constant. With the notations introduced in Fig. 6, the pressure and velocity fields can be written as

$$\begin{aligned}
p(x,y) &= \mu_l \frac{p_1 - p_0 - \sigma_{cap}}{h\mu_l + (1-h)\mu_a} y + p_0 && \text{in} \quad \Omega_l \\
p(x,y) &= \mu_a \frac{p_1 - p_0 - \sigma_{cap}}{h\mu_l + (1-h)\mu_a} (y-1) + p_1 && \text{in} \quad \Omega_a \\
v_x(x,y) &= 0 && \text{in} \quad \Omega \\
v_y(x,y) &= -K \frac{p_1 - p_0 - \sigma_{cap}}{h\mu_l + (1-h)\mu_a} && \text{in} \quad \Omega
\end{aligned} \tag{32}$$

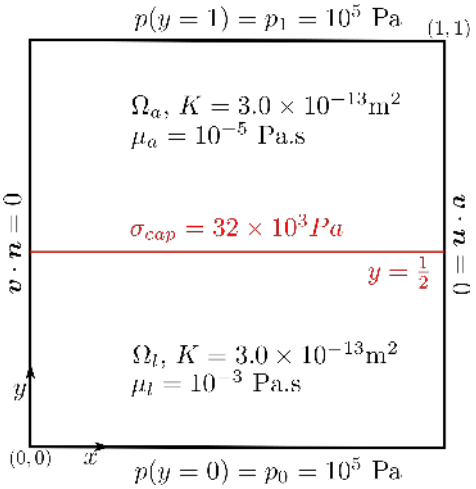

Figure 6: Material properties and boundary conditions used in the numerical simulation of unidirectional flow.

The velocity and pressure fields computed with a structured mesh of size $h_e = \frac{1}{50}$ (4800 triangular elements corresponding to 2499 nodes) and an interface crossing the elements, are given in Fig. 7 and 8. Two cases are considered: without and with the pressure enrichment introduced in section 2.4. In the first case, the pressure jump is not well-captured at the interface (Fig. 7(b)), resulting in a spurious velocity around this interface (Fig. 7(a)). On the contrary, the discontinuity of the pressure field is accurately computed with the enrichment (Fig. 8(b)) leading to a uniform velocity field as expected by Equation (Eq. 32) (Fig. 8(a)). Numerical and analytical values of the velocity are identical, and equal to 1.901×10^{-5} m.s^{-1} in norm. This also proves the accuracy of the pressure description. To complete this analysis, analytical and numerical pressures have been plotted on the line $\{x = \frac{1}{2}\}$ in Fig. 9, for different structured meshes. Again, no pressure oscillation is observed.

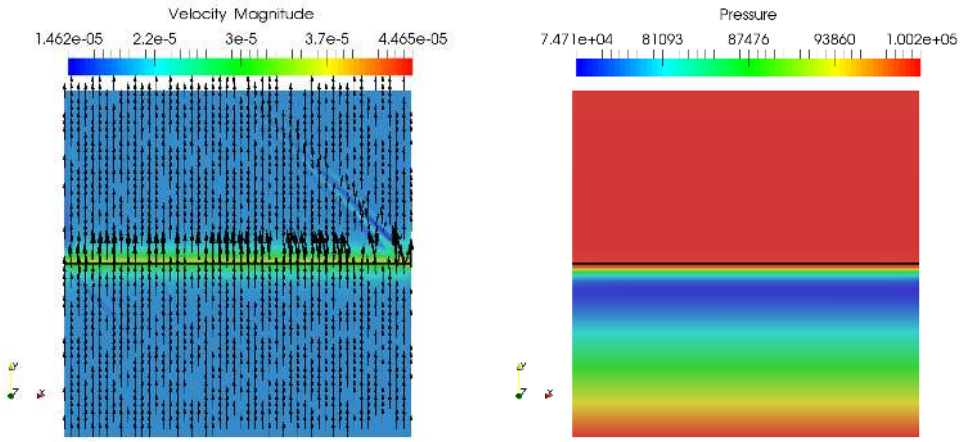

(a) Velocity (b) Pressure

Figure 7: Velocity and pressure fields obtained without pressure enrichment

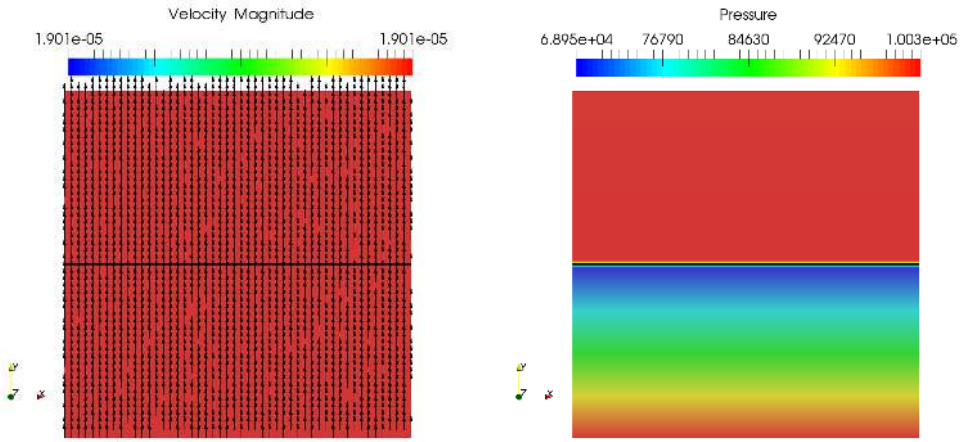

(a) Velocity (b) Pressure

Figure 8: Velocity and pressure fields obtained with pressure enrichment

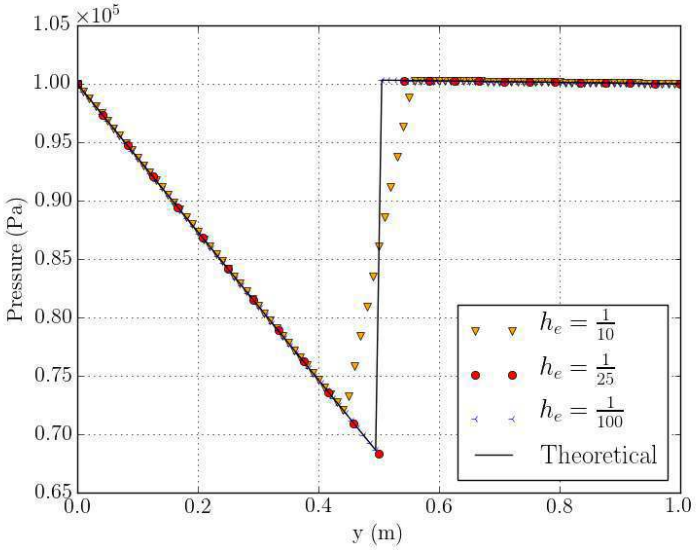

Figure 9: Comparison between analytical and numerical pressures, plotted along the line $\{x = \frac{1}{2}\}$, for different mesh sizes h_e.

5.2. Capillary wicking

In this section, simulation of wicking in carbon reinforcements is confronted to experimental data [62, 63]. The only driving force is thus due to capillary effects.

5.2.1. Experimental approach

Pucci *et al.* [62] proposed an experimental procedure to determine the scalar capillary stress σ_{cap} in the three main directions of a unidirectional (UD) carbon fabric (Fig. 11). On the one hand, for a given direction, the mass of water in the fabric $m(t)$ is recorded over time using a tensiometer. Wicking is commonly described by a modified Washburn equation [74] for porous media relating mass and time

$$m^2(t) = \left[\frac{(c\bar{r})\phi^2(\pi R^2)^2}{2}\right]\frac{\rho_l^2\gamma\cos\theta_a}{\mu_l}t \tag{33}$$

where c is a constant accounting for the tortuous path of liquid in the equivalent capillary tube arrangement of mean radius $\bar{r}$. ϕ is the porosity and R the inner radius of the cylindrical sample holder. The first term in square brackets finally represents a geometric factor of the porous medium. ρ_l and μ_l are, respectively, the liquid (water) density and its viscosity. θ_a is the apparent mean advancing contact angle during the capillary rise and γ_l the liquid surface tension.

On the other hand, from Darcy's equation applied to a unidirectional flow (Eq. 32) following the assumption of spontaneous impregnation under the effect of capillary stress σ_{cap} (Fig. 10) the square of the water height $h^2(t)$ (see Fig. 11) can be expressed as a function of time

$$h^2(t) = \frac{2K\sigma_{cap}}{\mu_l\phi}t \tag{34}$$

This expression is easily obtained from the last equation of the analytical model (Eq. 32), considering that $v_y = \phi\frac{dh}{dt}$, $p_1 = p_0$, $\mu_a = 0$ and integrating it with respect to time.

Taking into account the cylindrical shape of radius R, the mass gain can be related to the height by

$$m^2(t) = h^2(t)\phi^2\rho_l^2(\pi R^2)^2 \tag{35}$$

Considering the equivalence between Eq. 33 and Eq. 35, it is then possible to describe capillary stress σ_{cap} for a given permeability K [62].

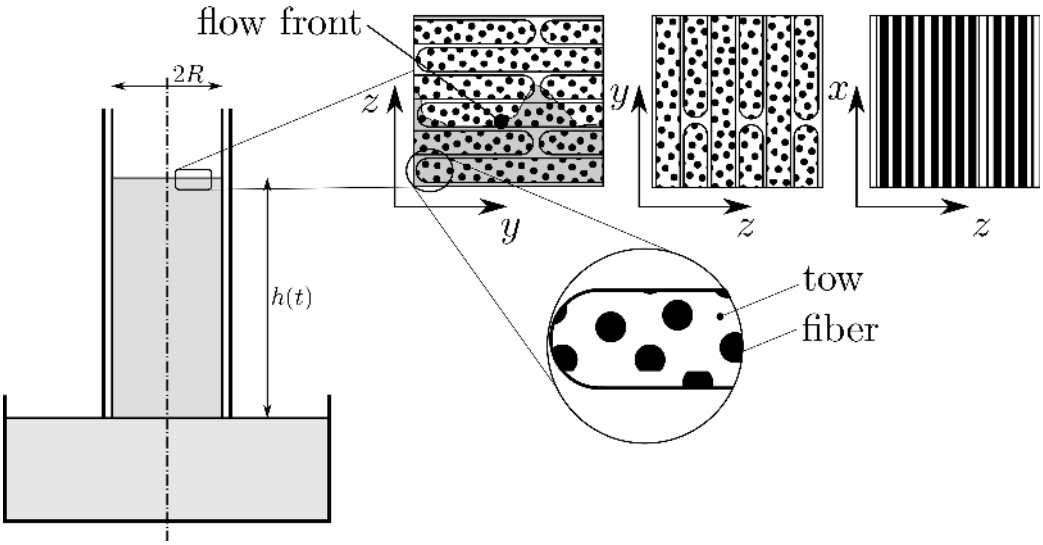

Figure 10: Capillary wicking in a cylindric quasi-UD carbon reinforcement according to Darcy law for the three principal directions of the medium.

5.2.2. Numerical simulations and results

Three 2D numerical simulations of wicking of water into a cylindrical quasi-UD carbon reinforcement have been carried out. For each simulation, the fabric is oriented in one of the directions x, y or z. Note that consequently, each of these simulations is reduced to an isotropic case. The computational domain, the $2R \times H$ rectangle described in Fig. 11, is discretized with a fixed mesh of $2,352$ triangular elements and $1,250$ nodes. The boundary conditions prescribed for this simulation are a zero normal velocity on the vertical sides and a pressure of 1 bar on the two other sides.

The definition of the orthotropic permeability tensor, orthotropic capillary stress tensor applied on the flow front and identified from experience, are given in Table 4, as well as the water and "air" viscosities, the water density, the porosity, and the dimensions $2R$ and H of the computational domain.

In order to have realistic simulations, the porosity has to be taken into account in Darcy's equations. This is achieved by substituting $\boldsymbol{v}\phi$ for $\boldsymbol{v}$ Darcy's equations. From the position of the water height $h(t)$ obtained by simulation, the corresponding water weight is calculated by Eq. 35 and compared (Fig. 12), with experimental data and the analytical expression given by Eq.

Permeabilities [49]	(m^2)
K_x	$3 \cdot 10^{-11}$
K_y	$1.5 \cdot 10^{-11}$
K_z	$3 \cdot 10^{-13}$
Capillary stress [62]	(kPa)
σ^x_{cap}	1.15±0.30
σ^y_{cap}	0.51 ± 0.14
σ^z_{cap}	32.10 ± 11.60
Others	
μ_{water}	10^{-3} Pa.s
ρ_{water}	10^3 kg.m^{-3}
μ_{air}	10^{-5} Pa.s
ϕ	0.40
$2R$	12 mm
H	20 mm

Table 4: Capillary wicking parameters.

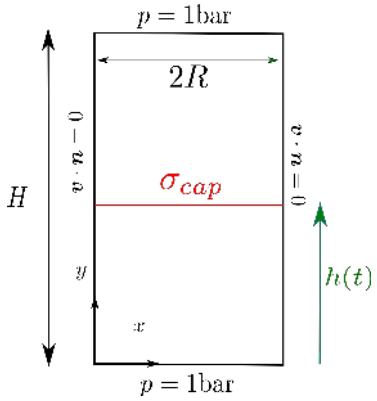

Figure 11: Geometrical parameters and boundary conditions of the capillary wicking.

34-35. It can be shown that numerical simulations and analytical expression give comparable results. Therefore, the numerical simulations reflect the experimental wicking. It confirms that the numerical model is correct since wicking in each main directions were already correctly described by the analytical model. However, the key point is that the proposed numerical methodology simulates wicking, a transient phenomenon, here in an isotropic context, but with realistic values of parameters involved in the model.

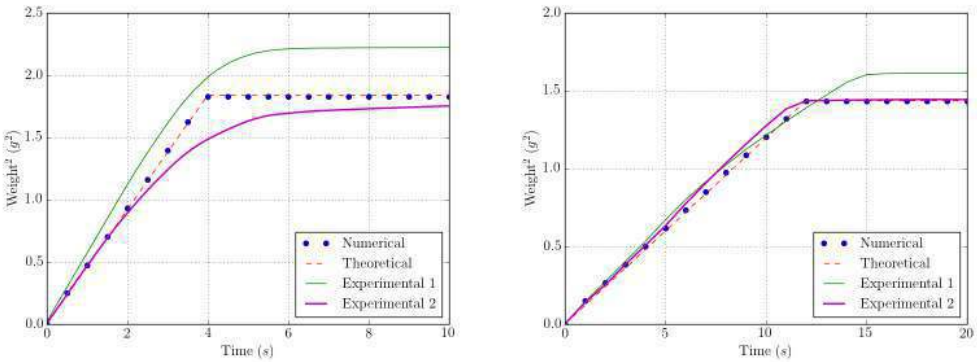

(a) (b)

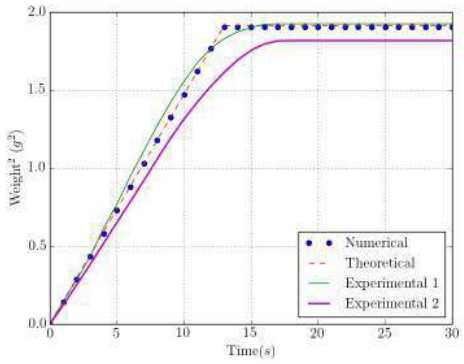

(c)

Figure 12: Comparison of the time dependent numerical and experimental weight in the x (a), y (b) and z (c) directions.

Parameters	Values	Units
K_t	10^{-14}	m^2
K_p	10^{-12}	m^2
σ^t_{cap}	0.3	bar
σ^p_{cap}	0.01	bar
μ_{resin}	0.1	Pa.s
μ_{air}	10^{-5}	Pa.s
ϕ	40%	
Δt	100	s

Table 5: Inputs - LRI simulation.

5.3. Full 3D-simulations of LRI process filling stage

This section investigates the 3D-simulation of the filling stage of a Liquid Resin Infusion (LRI) process [15, 22]. More precisely, the objective is to evaluate the influence of capillary effects on the resin impregnation. The part to be infused is the aeronautic-like stiffener shown in Fig. 13. Furthermore, the preform is assumed to have an additional symmetry: two eigen-values of the permeability tensor, as well as two eigen-values of the capillary stress tensor are equal. Hence, Table 5 gives the values of the in-plane permeability K_p, which is a hundred times larger than the transverse permeability K_t. As capillary forces are more significant in less permeable media, the capillary stress σ^t_{cap} in the transverse direction is higher than the value in the plan σ^p_{cap}. These values, completed by the resin viscosity, the air viscosity, the porosity and the time step Δt are also provided in Table 5. Figure 13 shows the corresponding materials eigen-directions y^t and x^p on a cutting plane. That is the transverse direction and the plane orthogonal to this direction in three different areas, allowing to compute numerical values of permeabilities and capillary stresses at each integration point of finite elements. Moreover, the boundary conditions both in velocity and pressure are given. The resin flow front is initialized as the plane $\{y = 0.5cm\}$. The flow is driven by the difference of pressure between the "inlet" (plane $\{y = 0\}$) and the "top" (plane $\{y = 12cm\}$) boundaries, equal to 10^5 Pa, and additionally by the capillary stress on $\Gamma_{l/a}$ when this is taken into account.

Regarding the solution for 1D cases, one may question about a simple way of accounting for capillary effects by modifying the overall pressure gradient. Although an extension to 3D is not straightforward, in order to assess

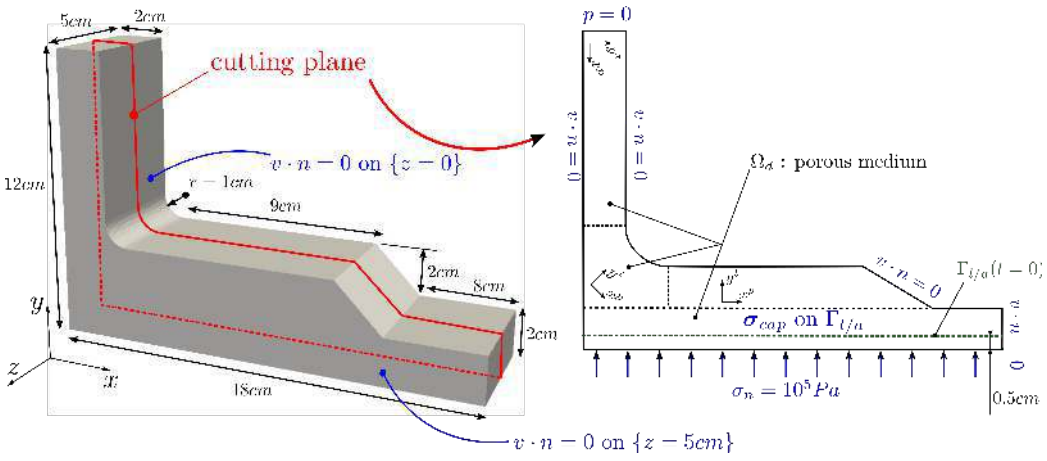

Figure 13: Geometrical dimensions and boundary conditions of the stiffener.

also such a basic approach, 3 simulations for the T-stiffener were considered: one carried out without capillary effects, one accounting for capillary effects by modifying the overall pressure gradient through changing the boundary condition in the plane $y = 0$: $\boldsymbol{n} \cdot \boldsymbol{\sigma} \cdot \boldsymbol{n} = 10^5\ Pa \rightarrow \boldsymbol{n} \cdot \boldsymbol{\sigma} \cdot \boldsymbol{n} = 10^5\ Pa + \sigma^t_{cap}$ - *Modified BC*-, and finally integrating orthotropic capillary stresses with the proposed method - *Discontinuous Pressure*-. Figure 14 compares the flow front position during infusion for the corresponding three simulations. As expected, the part is filled more quickly when the capillary effects are taken into account: 1h58 min with the Modified BC approach using the highest capillary stress σ^t_{cap}, 2h 10min with our discontinuous pressure numerical model and 3 hours without any capillary effects. One can verify that capillary effects will help the filling of the preform. Besides, the pressure and fluid front kinetics resulting from the approaches integrating these effects differ largely.

More precisely, the pressure computed from the 3 methods are presented in Figure 15, for locations along a vertical line $\{0.01; y; 0.2\}$ as sketched in Figure 14b. One can verify that the pressure profiles obtained without capillary effects and with the Discontinuous Pressure method are quite close, showing the ability of the latter method to capture properly the pressure field out of the interface region (pressure gradient) while integrating locally the capillary effects. As for the Modified BC, the obtained pressure profile is largely modified. Also, it can be noticed that the Discontinuous Pressure approach yields

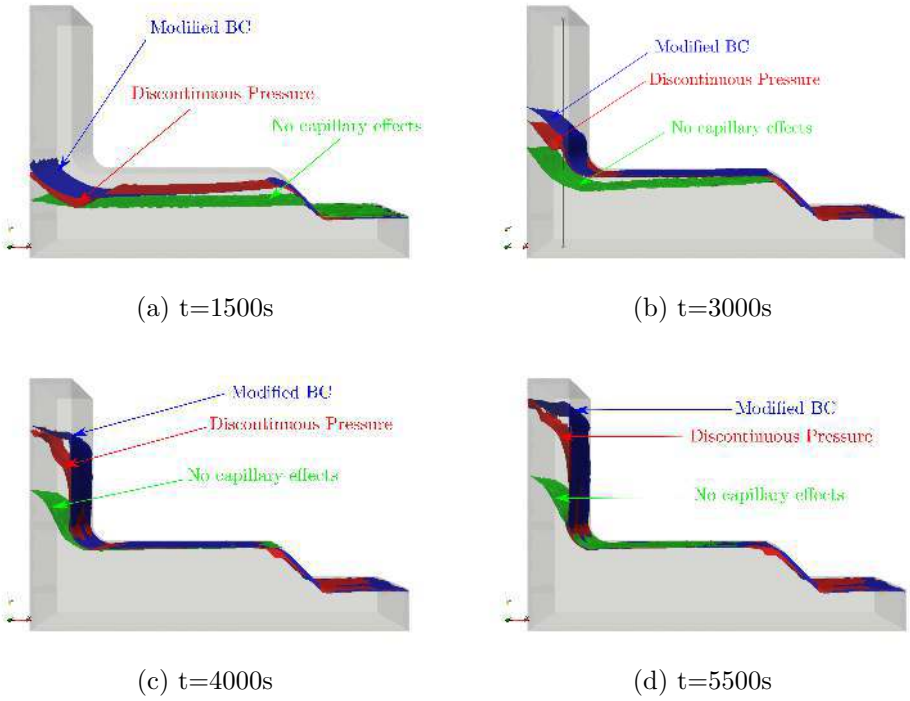

(a) t=1500s (b) t=3000s

(c) t=4000s (d) t=5500s

Figure 14: Numerical results - position of the fluid front during the filling of an orthotropic stiffener at different times

a pressure jump whose magnitude is a combination of both capillary stresses in the transverse and plane directions. This method is intrinsically able to account for the capillary stress orthotropy, and the corresponding flow front follows the preform principal directions.

It can be concluded that with the Modified BC method, first the orthotropic character of the capillary effects will not be accounted for by the simple overall gradient correction, and second the pressure field will not be discontinuous, opposite to the physics of two-phase flows. Consequently, a finer analysis is not possible with this approach, and especially it will no longer hold for a more exhaustive modelling approach relying on velocity and fluid pressure fields. Conversely, the proposed approach with discontinuous pressure will yield relevant pressure and velocity distributions which can then be incorporated in more exhaustive approaches of the filling stage including solid-fluid mechanics couplings through the fluid pressure. Of course,

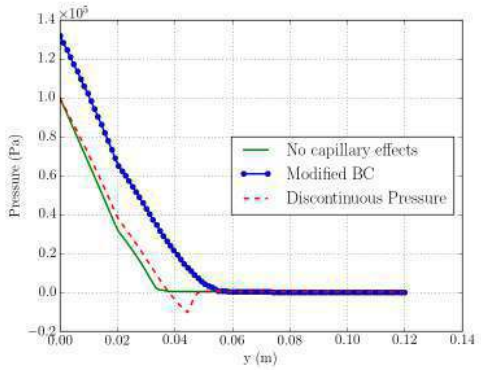

Figure 15: Comparison of the pressure fields with the *Modified BC - Discontinuous Pressure* methods and without capillary effects at t=3000s along a vertical line $\{0.01; y; 0.2\}$ plotted in Fig. 14b.

further experimental studies are required to validate and calibrate the numerical model for industrial-like structures. However, these results show that capillary effects may have huge impact on the filling strategy for the out-of-autoclave processes targeted here.

6. Conclusion

In our macroscale configuration, the capillary action is represented by capillary stresses, acting at the liquid/air interface by the mean of the normal vector. This stress is weakly enforced in Darcy's equations as an input parameter of the model and generates a pressure jump at the interface. These equations are discretized using a stabilized mixed FE method, linear in both velocity and pressure. The spurious velocities due to the pressure discontinuity are limited by using a local pressure enrichment technique. The numerical model gives the expected convergence rates, both for velocity and pressure. Besides, the 2D isotropic simulations of a capillary wicking of water inside a carbon fabric show a good correlation between the numerical results and the experimental data, as well as with the analytical model of Washburn's equation. Finally, a full 3D and orthotropic case has been investigated: the filling of an aeronautic part with a LRI process. This simulation enlightens the influence of the capillary effects on the progress of the filling stage, and demonstrates that the overall response is of highest importance, but also the

proper representation of the pressure discontinuity is mandatory for velocity and pressure fields predictions to be used for solid-fluid mechanics couplings for instance [15]. Further experimental studies are now required in order to confirm this scenario.

[1] J. Aarnes and B. Heimsund. Multiscale discontinuous galerkin methods for elliptic problems with multiple scales. In B. Engquist, O. Runborg, and P. Lötstedt, editors, Multiscale Methods in Science and Engineering, pages 1–20. Springer Berlin Heidelberg, 2005.

[2] L. Abouorm, M. Blais, N. Moulin, J. Bruchon, and S. Drapier. A robust monolithic approach for resin infusion based process modelling. Key Engineering Materials, 611-612:306–315, 2014.

[3] L. Abouorm, R. Troian, J. Bruchon, and S. Drapier. Stokes/Darcy coupling in severe regimes using multiscale stabilization for mixed finite element: monolithic approach versus decoupled approach. European Journal of Computational Mechanics, 23:113–137, 2014.

[4] S. Afkhami, Z. Zaleski, and M. Bussman. A mesh-dependent model for applying dynamic contact angles to vof simulations. Journal of Computational Physics, 228:5370–5389, 2009.

[5] K. J. Ahn, J. C. Seferis, and J. C. Berg. Simultaneous measurements of permeability and capillary pressure of thermosetting matrices in woven fabric reinforcements . Polymer Composites, 12:146–152, 1991.

[6] R. Ausas, G. C. Buscaglia, and S. R. Idelsohn. A new enrichment space for the treatment of discontinuous pressures in multi-fluid flows. International Journal for Numerical Methods in Fluids, 70:829–850, 2011.

[7] S. Badia and R. Codina. On a multiscale approach to the transient Stokes problem: Dynamic subscales and anisotropic space-time discretization. Applied Mathematics and Computation, 207:415–433, 2009.

[8] S. Badia and R. Codina. Unified stabilized finite element formulations for the Stokes and the Darcy problems. SIAM Journal of Numerical Analysis, 47:1971–2000, 2009.

[9] S. Badia and R. Codina. Stabilized continuous and discontinuous Galerkin techniques for Darcy flow. Computer Methods in Applied Mechanics and Engineering, 199:1654–1667, 2010.

[10] S. Badia and R. Codina. Stokes, Maxwell and Darcy: a single finite element approximation for three model problems. Applied Numerical Mathematics, 62:246–263, 2012.

[11] T. A. Baer, R. A. Cairncross, P. R. Schunk, R. R. Rao, and P. A. Sackinger. A finite element method for free surface flows of incompressible fluids in three dimensions. Part II: Dynamic wetting lines. International Journal of Numerical Methods in Fluids, 33:405–427, 2000.

[12] P. Bastian. A fully-coupled discontinuous Galerkin method for two-phase flow in porous media with discontinuous capillary pressure. Computational Geosciences, 18:779–796, 2014.

[13] L. Benazzouk, E. Arquis, N. Bertrand, C. Descamps, and M. Valat. Motion of a liquid bridge in a capillary slot: a numerical investigation of wettability and geometrical effects. La Houille Blanche, 3:50–56, 2013.

[14] C. Binetruy, J. Pabiot, and B. Hilaire. The influence of fiber wetting in resin transfer molding: scale effects. Polymer Composites, 21(4):548–557, 2000.

[15] M. Blais, N. Moulin, P.-J. Liotier, and S. Drapier. Resin infusion-based processes simulation : coupled Stokes-Darcy flows in orthotropic preforms undergoing finite strain. International Journal of Material Forming, 10(1):43–54, 2017.

[16] J. U. Brackbill, D. B. Kothe, and C. Zemach. A continuum method for modeling surface tension. Journal of Computational Physics, 100:335–354, 1992.

[17] J. Bréard, A. Saouab, and G. Bouquet. Numerical simulation of void formation in lcm. Composites: Part A, 34:517–523, 2003.

[18] F. Brezzi, T. J. R. Hughes, L. D. Marin, and A. Masud. Mixed Discontinuous Galerkin methods for Darcy flow. Journal of Scientific Computing, 22(1-3):119–145, 2005.

[19] A. N. Brooks and T.J.R Hughes. Streamline upwind/Petrov-Galerkin formulations for convection dominated flows with particular emphasis on the incompressible Navier-Stokes equations. Computer Methods in Applied Mechanics and Engineering, 32(1):199–259, 1982.

[20] G. Buscaglia and R. Ausas. Variational formulations for surface tension capillarity and wetting. Computational Methods Applied Mechanical Engineering, 200(45-46):3011–3025, 2011.

[21] T. Carraro and S. Wetterauer. On the implementation of the eXtended finite element method (XFEM) for interface problems. Archive of Numerical Software, 4(2):1–23, 2016.

[22] P. Celle, S. Drapier, and J-M. Bergheau. Numerical modelling of liquid infusion into fibrous media undergoing compaction. European Journal of Mechanics -Part A: Solids, 27(4):647–661, 2008.

[23] J. Chessa and T. Belytschko. An eXtended finite element method for two-phase fluids. Transaction of the ASME, 70:10–17, 2003.

[24] L. Chevalier, N. Moulin, P-J. Liotier, J. Bruchon, and S. Drapier. Accounting for local capillary effects in two-phase flows with relawed surface tension formulation in enriched finite element. Preprint, 2018.

[25] R. Codina. On stabilized finite element methods for linear systems of convection-diffusion-reaction equations. Computer Methods in Applied Mechanics and Engineering, 182:61–82, 2000.

[26] H. Coppola-Owen and R. Codina. Improving eulerian two-phase on finite element approximation with discontinuous gradient pressure shape functions. International Journal for Numerical Methods in Fluids, 49:1287–1304, 2005.

[27] T. Coupez, L. Silva, and E. Hachem. Implicit Boundary and Adaptive Anisotropic Meshing, pages 1–18. Springer International Publishing, 2015.

[28] H. Darcy. Les fontaines publiques de la ville de Dijon. Paris: Victor Dalmont, 1856.

[29] A. Dereims, S. Drapier, J-M. Bergheau, and P. De Luca. 3D robust iterative coupling for Stokes, Darcy and solid mechanics for low permeability media undergoing finite strains. Finite Element Analysis, 94:1–15, 2015.

[30] M. Discacciati, D. Hacker, A. Quarteroni, S. Quinodoz, S. Tissot, and F. M. Wurm. Numerical simulation of orbitally shaken viscous fluids with free surface. International Journal for Numerical Methods in Fluids, 71(3):294–315, 2013.

[31] T.-P. Fries and T. Belytschko. The extended/generalized finite element method: An overview of the method and its applications. International Journal for Numerical Methods in Engineering, 84(3):253–304, 2010.

[32] A. Fumagalli and A. Scotti. An efficient XFEM approximation of Darcy flows in arbitrarily fractured porous media. Oil & Gas Science and Technology, 69(4):555–564, 2014.

[33] S. Ganesan, G. Matthies, and Tobiska L. On spurious velocities in incompressible flow problems with interfaces. Computer Methods in Applied Mechanics and Engineering, 196:1193–1202, 2007.

[34] G. N. Gatica, R. Oyarzua, and F-J. Sayas. Analysis of fully-mixed finite element methods for the Stokes-Darcy coupled problem. Mathematics of Computation, 276:1911–1948, 2011.

[35] C. Geuzaine and J. F. Remacle. Gmsh: a three-dimensional finite element mesh generator with built-in pre- and post-processing facilities. International Journal for Numerical Methods in Engineering, 79(11):1309–1331, 2009.

[36] Q. Govignon, S. Bickerton, and P. A. Kelly. Simulation of the reinforcement compaction and resin flow during the complet resin infusion process. Composites Part A: Applied Science and Manufacturing, 41(1):45–57, 2010.

[37] O. Guasch and R. Codina. An algebraic subgrid scale finite element method for the convected Helmholtz equation in two dimensions with applications in aeroacoustics. Computer Methods in Applied Mechanics and Engineering, 196:4672–4689, 2007.

[38] R. Helmig, Weiss A., and B. I. Wohlmuth. Dynamic capillary effects in heterogeneous porous media. Computational Geosciences, 11(3):261–274, 2007.

[39] T. J. R. Hughes. Multiscale phenomena: Green's functions, the Dirichlet-to-Neumann formulation, subgrid scale models, bubbles, and the origins of stabilized methods. Computer Methods in Applied Mechanics and Engineering, 127:387–401, 1995.

[40] T. J. R. Hughes. The variational multiscale method - A paradigm for computational mechanics. Computer Methods in Applied Mechanics and Engineering, 166(1-2):3–24, 1998.

[41] T. J. R. Hughes, A. Masud, and J. Wan. A stabilized mixed Discontinuous Galerkin method for Darcy flow. Computer Methods in Applied Mechanics and Engineering, 195(25-28):3347–3381, 2006.

[42] S. R. Idelsohn, J. M. Gimenez, J. Marti, and N. M. Nigro. Elemental enriched spaces for the treatment of the weak and strong discontinuous fields. Computational Methods Applied Mechanical Engineering, 313:535–559, 2017.

[43] S. R. Idelsohn, J. M. Gimenez, and N. M. Nigro. Multifluid flows with weak and strong discontinuous interfaces using an elemental enriched space. International Journal for Numerical Methods in Fluids, pages n/a–n/a. accepted for publication, DOI: 10.1002/fld.4477.

[44] S. R. Idelsohn, N. Mier-Torrecilla, N. Nigro, and E. Onate. On the analysis for heterogenous fluids with jumps in the viscosity using a discontinuous pressure field. Computational Mechanics, 46(1):115–124, 2010.

[45] Y. Jung, S. J. Kim, and W. S. Han. Numerical simulation of RTM process using the extended finite element method combined with the level set method. Journal of Reinforced Plastics and Composites, 32:308–317, 2013.

[46] S. Koubaa, C. Burtin, and S. Le Corre. Investigation of capillary impregnation for permeability prediction of fibrous reinforcements. Journal of Composite Materials, 50(11):1417–1429, 2016.

[47] D. Krauss. Two-phase flow in homogeneous porous media - The role of dynamic capillary pressure in modeling gravity driven fingering. Master's thesis, 2011.

[48] S. Lee and M. F. Wheeler. Enriched Galerkin methods for two-phases flow in porous media with capillary pressure. arXiv preprint arXiv:1709.01644, 2017.

[49] M. Li, S. K Wang, Y. Z Gu, K. Potter, and Z. G. Zhang. Evaluation of through-thickness permeability and the capillary effect in vaccum assisted liquid molding process. Composites Science and Technology, 72(8):873–878, 2012.

[50] Y. Liu, L. Wang, X. Liu, and T. Ding. Effects of capillary pressure - fluid saturation - relative permeability relationships on predicting carbon dioxide migration during injection into saline aquifers. Energy Procedia, 63:3616–3631, 2014.

[51] R. Lucas. Rate of capillary ascension of liquids. Kollid Z, 23:15–22, 1918.

[52] R. Masoodi and K. M. Pillai. Wicking in Porous Materials - Traditional and Modern Approaches. CRC Press, 2012.

[53] A. Masud and T. J. R. Hughes. A stabilized mixed finite element method for Darcy flow. Computer Methods in Applied Mechanics and Engineering, 191(25-28):4341–4370, 2002.

[54] V. Michaud and A. Mortensen. Infiltration processing of fibre reinforced composites: governing phenomena. Composites: Part A, 32:98–996, 2001.

[55] P. D. Minev, T. Chen, and K. Nandakumar. A finite element technique for multifluid incompressible flow using Eulerian grids. Journal of Computational Physics, 187(255-273), 2003.

[56] A. Monlaur, S. Fernandez-Mendez, and A. Huerta. Discontinuous Galerkin methods for the Stokes equations using divergence-free approximations. International Journal for Numerical Methods in Fluids, 57:1071–1092, 2008.

751 [57] S. Osher and R. P. Fedkiw. Level set methods: an overview and some
752 recent results. Journal of Computational Physics, 169(2):463–502, 2000.

753 [58] G. Pacquaut, J. Bruchon, N. Moulin, and S. Drapier. Combining a levet-
754 set method of mixed stabilized p1/p1 formulation for coupling Stokes-
755 Darcy flows. International Journal of Numerical Methods in Fluids,
756 69(2):459–480, 2012.

757 [59] C. H. Park, A. Lebel, A. Saouab, J. Brard, and W. Lee. Modeling and
758 simulation of voids and saturation in liquid composite molding processes.
759 Composites Part A: Applied Science and Manufacturing, 42(6):658–668,
760 2011.

761 [60] R. S. Pierce, B. G. Falzon, and M. C. Thompson. A multi-physics pro-
762 cess model for simulating the manufacture of resin - infused composite.
763 Composites Science and Technology, 149:269–279, 2017.

764 [61] D. Pino Muñoz, J. Bruchon, S. Drapier, and F. Valdivieso. A finite ele-
765 ment based level set method for fluid-elastic solid interaction with sur-
766 face tension. International Journal for Numerical Methods Engineering,
767 93(9):919–941, 2013.

768 [62] M. F. Pucci, P-J. Liotier, and S. Drapier. Capillary wicking in a fibrous
769 reinforcement - orthotropic issues to determine the capillary pressure
770 components. Composites/A, 77:133–141, 2015.

771 [63] M. F. Pucci, P-J. Liotier, and S. Drapier. Capillary wicking in
772 flax fabrics - effects of swelling in water. Colloids and Surfaces/A:
773 Physicochemical and Engineering Aspects, 498:176–184, 2016.

774 [64] P. J. Roache. Code verification by the method of manufactured solutions.
775 Journal of Fluids Engineering, 124(1):1–4, 2002.

776 [65] P. Simacek and S. G. Advani. A numerical model to predict fiber tow
777 saturation during liquid composite molding. Composites Science and
778 Technology, 63(12):1725–1736, 2003.

779 [66] P. Simacek and S. G. Advani. Desirable features in mold filling sim-
780 ulations for liquid composite molding processes. Polymer Composites,
781 25:355–367, 2004.

[67] P. Simacek, V. Neacsu, and S. G. Advani. A phenomenological model for fiber tow saturation of dual scale fabrics in liquid composite molding. Polymer Composites, 31(11):1881–1889, 2010.

[68] Zset Software. http://www.zset-software.com/.

[69] M. Toure. Stabilized finite element method for solving the level set equation without reinitialization. Journal Computers & Mathematics with Applications, 71(8):1602–1623, 2016.

[70] J. Verrey, V. Michaud, and J.-A. E. Manson. Dynamic capillary effects in liquid composite molding with non-crimp fabrics. Composite Part/A, 37(1):92–102, 2006.

[71] Š. Šikalo, H.-D. Wilhelm, I. V. Roisman, S. Jakirlić, and C. Tropea. Dynamic contact angle of spreadin droplets: experiments and simulations. Physics of Fluids, 17(6):062103, 2005.

[72] Y. Wang, M. Moatamedi, and S. M. Grove. Continuum dual-scale modeling of liquid composite molding processes. Journal of Reinforced Plastics and Composites, 28, 2009.

[73] E. W. Washburn. The dynamics of capillary flow. Physics Reviews, 17:273–283, 1921.

[74] E. W. Washburn. Note on a method of determining the distribution of the pore sizes in porous material. Proceedings of the National Academy of Sciences USA, 7(4):115–116, 1921.

[75] J. Yang, Y. Jia, S. Sun, D. Ma, T. Shi, and L. An. Mesoscopic simulation of the impregnation process of unidirectional fibrous preform in Resin Transfer Molding. Materials Science and Engineering A, pages 515–520, 2006.

[76] M. Yeager, W. R. Hwang, and S. G. Advani. Prediction of capillary pressure for resin flow between fibers. Composites Science and Technology, 126:130–138, 2016.